


## PAPER

[View Article Online](#)  
[View Journal](#) | [View Issue](#)Cite this: *Nanoscale*, 2024, **16**, 6984

# GO-tagged PEI sizing agent imparts self-healing and excellent mechanical properties to carbon fiber reinforced epoxy laminates†

Samir Mandal, Ketaki Samanta,  \* Kunal Manna,  Subodh Kumar\* and Suryasarathi Bose  \*

Carbon fiber-reinforced epoxy (CFRE) laminates have attracted significant attention as a structural material specifically in the aerospace industry. In recent times, various strategies have been developed to modify the carbon fiber (CF) surface as the interface between the epoxy matrix and CFs plays a pivotal role in determining the overall performance of CFRE laminates. In the present work, graphene oxide (GO) was used to tag a polyetherimide (PEI, termed BA) containing exchangeable bonds and was employed as a sizing agent to improve the interfacial adhesion between CFs and epoxy. This unique GO-tagged-BA sizing agent termed BAGO significantly enhanced the mechanical properties of CFRE laminates by promoting stronger interactions between CFs and the epoxy matrix. The successful synthesis of BAGO was verified by Fourier-transform infrared spectroscopy. Additionally, the partial reduction of GO owing to this tagging with BA was further confirmed by X-ray diffraction and Raman spectroscopy, and the thermal stability of this unique sizing agent was evaluated using thermogravimetric analysis. The amount of GO in BAGO was optimized as 0.25 wt% of BA termed 0.25-BAGO. The 0.25-BAGO sizing agent resulted in a significant increase in surface roughness, from 15 nm to 140 nm, and surface energy, from 13.2 to 34.7 mN m<sup>-1</sup> of CF. The laminates prepared from 0.25-BAGO exhibited a remarkable 40% increase in flexural strength (FS) and a 35% increase in interlaminar shear strength (ILSS) due to interfacial strengthening between epoxy and CFs. In addition, these laminates exhibited a self-healing efficiency of 51% in ILSS due to the presence of dynamic disulfide bonds in BAGO. Interestingly, the laminates with 0.25-BAGO exhibited enhanced Joule heating and enhanced deicing, though the EMI shielding efficiency slightly declined.

Received 28th November 2023,  
Accepted 19th February 2024

DOI: 10.1039/d3nr06047k

[rsc.li/nanoscale](https://rsc.li/nanoscale)

## 1. Introduction

Carbon fiber reinforced epoxy (CFRE) laminates find extensive application in various aircraft components due to their remarkable strength-to-weight ratio, impressive mechanical properties, effective resistance against corrosion, high stiffness, damping characteristics, and consequential benefits such as reduced fuel consumption and lower assembly expenses in the aviation industry.<sup>1,2</sup> The additional attributes, which are crucial for assessing their effectiveness in these applications, are electromagnetic interference (EMI) shielding, lightning protection, and deicing.<sup>3,4</sup> The interfacial interactions between carbon fibers (CFs) and epoxy play a crucial role in determining these properties. The smooth and inert

surface of CFs results in a weak mechanical interlocking and poor wettability between CFs and the epoxy matrix eventually leading to delamination failure.<sup>5–8</sup> Hence, interfacial strengthening is key to improving the overall performance of CFRE laminates.

Several strategies have been adopted to modify the surface of CFs, including plasma treatment,<sup>9</sup> chemical functionalization,<sup>10</sup> chemical grafting,<sup>11</sup> sizing<sup>12</sup> and so on. However, some modification needs harsh environments, which introduce defects in CFs. Sizing stands out as a cost-effective and controllable approach among these methods. It aims to apply a polymer coating to safeguard CFs from getting fluffy and damaged during their production and use.<sup>13</sup> Furthermore, sizing agents impart functional groups over CFs. These functional groups facilitate a strong chemical interaction between the sized modified fiber and the resin at the interface.<sup>14</sup> Zhang *et al.* have investigated the effect of various epoxies as a sizing agent on IFSS.<sup>15</sup> Sizing agents like oligomeric siloxanes<sup>16</sup> and *in situ* polymerized HTPB-based di-block copolymers<sup>17</sup> have

Department of Materials Engineering, Indian Institute of Science, Bangalore, 560012 India. E-mail: [ketakisamanta123@gmail.com](mailto:ketakisamanta123@gmail.com), [skumar@iisc.ac.in](mailto:skumar@iisc.ac.in), [sbose@iisc.ac.in](mailto:sbose@iisc.ac.in)  
† Electronic supplementary information (ESI) available. See DOI: <https://doi.org/10.1039/d3nr06047k>

been used in earlier studies. The use of the above-mentioned sizing agents was associated with a significant improvement in IFSS and ILSS (70%). Liu *et al.* synthesized a dendrimer structure on the CF surface that forms entanglements and chemical bonds with the matrix, resulting in an improvement in ILSS (42%), IFSS (82%), and impact strength (24%).<sup>18</sup> However, the acid and oxidative treatments were still required as a preliminary step. Furthermore, the low thermal stability and poor compatibility with the matrix limit the application of sizing agents on CFRE.<sup>19</sup>

With advancements in nanotechnology, incorporating nanoparticles has improved fiber-matrix adhesion in CFRE. There are two strategies to introduce nanoparticles in CFRE; first can be described by dispersion in the matrix, which brings some process difficulties like enhancing the viscosity, percentage of shrinkage, *etc.*<sup>20,21</sup> However, the good distribution of nanomaterials at the interface reduces these problems along with improving mechanical interlocking and the chemical interaction with the matrix. Functionalized carbon nanotubes (MWCNTs)<sup>22</sup> and graphene oxide (GO)<sup>23</sup> are commonly used 1D and 2D carbon-based nanoparticles to enhance the interfacial interactions. Additionally, oxygen-containing polar groups on the surface of functionalized MWCNTs and GO facilitate interfacial interactions *via* non-covalent or covalent bonds with CFs and the matrix during processing. Qin *et al.* observed that graphene-coated CF/epoxy composites had flexural strength and through-thickness conductivity that were 82% and 165% higher than those of neat CF/epoxy composites.<sup>24</sup> Zhang *et al.* synthesized halloysite nanotubes and chemically grafted them on the surface of CFs and observed

11% and 16% improvement in ILSS and IFSS with improvement in hydrothermal aging.<sup>25</sup> Parasuram *et al.* synthesized hybrid CNT-GO nanomaterials and deposited them on CFs electrophoretically.<sup>26</sup> This unique strategy enhanced ILSS by 30% but still agglomeration was a major issue with this method. However, to overcome the dispersion difficulties, researchers have adopted the covalent and non-covalent methods.<sup>27,28</sup>

In CFRE laminates, several failure modes have been observed, including interfacial delamination, matrix cracking, and fiber breakage.<sup>29,32</sup> Sometimes, unreparable small cracks and delamination are the reason for completely discarding the whole section. Therefore, self-healing materials are being introduced at the interface for the damaged structure to repair itself. Extrinsic and intrinsic are the two types of self-healing approaches. Extrinsic mechanisms contain external agents like microcapsules<sup>30,31</sup> and hollow fibers,<sup>32,33</sup> which contain healing materials that are released on rupture and fill the crack. However, low healing cycles and processing difficulties constrained this mechanism. Intrinsic self-healing, on the other hand, makes use of dynamic chemical structures that re-join covalent bonds and aid in self-healing in response to a stimulus like heat. Dynamic covalent bonds (DCBs) can separate and recombine at a particular temperature. The material's innate capacity to re-join broken linkages gives it self-healing characteristics. DCBs are further classified into dissociative (Diels–Alder, triazolium, pyridinium exchange, *etc.*) and associative (transesterification, disulfide metathesis, boroxine, silyl ether, thio-ether, diketo-enamin, sulfonium, imine exchange, *etc.*) covalent adaptable networks (CANs). Zhang *et al.* fabricated a thermoreversible Diels–Alder based polymer composite with 60% self-healing efficiency, but it was observed that property consistency was a major issue after each healing cycle.<sup>34</sup> Banerjee *et al.* reported a 70% healing efficiency in a GO–BMI-modified CFRE laminate using the Diels–Alder mechanism.<sup>35</sup> However, the network topology was lost due to the dissociative mechanism, which involved breaking DCBs and re-joining at various points throughout the network. On the other hand, through the associative CAN mechanism, the exchange of dynamic bonds occurs at different points without distinctly separate dissociation and re-association processes, keeping the structural integrity unaltered within the DCB system. As a result, the network topology and intrinsic viscosity are not disrupted in the associative CAN, leading to consistency in properties for associative CAN.<sup>36,37</sup>

We have sized CFs with polyetherimide (PEI), which was synthesized from 4,4'-(4,4'-isopropylidenediphenoxy) bis(phthalic anhydride) (BPADA) and 4-aminophenyl disulfide (AFD), which was termed BA. CFRE laminate prepared from CFs sized with 0.25 wt% BA of CFs exhibited a 19% increase in FS and a 26% increase in ILSS with 50% self-healing efficiency in ILSS. We have now tagged GO to BA and this sizing agent termed BAGO was used to modify the surface of CFs to further improve the mechanical properties and self-healing efficiency of CFRE laminates. These results are presented and analysed in this manuscript.



**Ketaki Samanta**

*Dr Ketaki Samanta received her M.Sc. degree in chemistry from Vidyasagar University, West Bengal, India in 2013. Subsequently, she completed her PhD thesis titled 'Nanocomposite of Syndiotactic Polystyrene with Conducting Polymer: Structure and Properties', at the Indian Association for the Cultivation of Science (IACS), Kolkata, India in 2022. She was selected as a Newton Bhabha Fellow and worked at Durham University,*

*UK as a part of her PhD. Currently Dr Samanta is working as a Postdoctoral Fellow in the Department of Materials Engineering, Indian Institute of Science (IISc), Bangalore. Also, she is a visiting researcher at Brunel University, London as a part of collaboration. Her research interests include polymer nanocomposites, polymer processing, carbon fiber composites, electrochemistry, organic synthesis, sustainable materials, polymer recycling through vitrimer chemistry, synthesis of bioplastics, etc. She has published 11 research articles in her field.*

## 2. Materials

Dygidyl ether of bisphenol-A type epoxy (DGEBA) resin and aromatic amine-based curing agents were procured from Atul Industry. Bhor Chemical supplied a bi-directional CF mat with a fiber diameter of approximately 7  $\mu\text{m}$  and a GSM of 200. 4-Aminophenyl disulfide (AFD), 4,4'-(4,4'-isopropylidenediphenoxy) bis(phthalic anhydride) (BPADA), and *N*-methyl-2-pyrrolidone (NMP) solvents used for the synthesis of PEI were acquired from Sigma Aldrich. Graphene oxide (GO) flex was procured from Nano Matrix Materials. Acetone used to desize CFs and a spray gun were sourced from local vendors, while the necessary consumables for the VARTM process were sourced from Amtek International.

## 3. Experimental procedure

### 3.1. Synthesis of BAGO

In the present work, a PEI macromolecule was synthesized from BPADA and AFD to yield PEI termed BA. The BPADA was mixed with AFD powder at a 1.5/1 molar ratio, and the solution was dissolved in NMP solvent to form 20 wt% solution. This solution was subjected to magnetic stirring for 24 h under a nitrogen atmosphere to form initial polyamic acid (PAA). GO was also dispersed in NMP solvent in another beaker by probe sonication followed by magnetic stirring. Then, the GO solution was poured into the PAA solution, and a continuous stirring was carried out for 6 h to get a uniform dispersion of GO in the PAA solution. The final step was to transfer the entire solution to a Petri dish and heat it in a hot air oven (250  $^{\circ}\text{C}$ ) for 15 minutes to imidize the solution and obtain GO-tagged-BA termed BAGO here. In this study, three different amounts of GO, *i.e.*, 0.25 wt%, 0.5 wt% and 1 wt% of BA, were used and the resulting BAGO is termed 0.25-BAGO, 0.5-BAGO and 1-BAGO, respectively. The complete process of synthesis and reaction scheme of BAGO is shown in Fig. 1.

### 3.2. Modification of CFs

Commercial CF-mat has a small amount of epoxy sizing over it. To remove epoxy sizing, CF-mat was soaked in acetone for 48 h at room temperature to desize it and then dried. Desized and dried CF-mats were spray coated with 10% w/v NMP solution containing BAGO and dried in a hot air oven for 6 h at 100  $^{\circ}\text{C}$ . CF sized with 0.25-BAGO, 0.5-BAGO and 1-BAGO is referred to as 0.25-BAGO-CF, 0.5-BAGO-CF, and 1-BAGO-CF, respectively.

### 3.3. Fabrication of CFRE laminates

As prescribed by the supplier, the resin was mixed with the hardener in a ratio of 100:24 and magnetically mixed for 20 minutes. The hardener was degassed at 1 bar under vacuum for 15 minutes. This degassing was done to remove the trapped air during the mixing process. Ten layers of CF mats were stacked on top of each other with 0 $^{\circ}$  orientation on a glass plate coated with the release film & peel ply. A mesh was placed atop the stacked fibers to facilitate resin infusion. Subsequently, the entire setup was vacuum bagged, and resin was infused into it. The CF-mat was impregnated with the

resin by applying a pressure of 28 mm Hg through a VARTM process. The resulting laminate was then subjected to a curing cycle at 80  $^{\circ}\text{C}$  for 2 h, then 100  $^{\circ}\text{C}$  for 2 h, then 120  $^{\circ}\text{C}$  for 2 h, and finally at 150  $^{\circ}\text{C}$  for 4 h in a hot air oven. As received CF laminate is referred to as neat CFRE. Laminates prepared from 0.25-BAGO-CF, 0.5-BAGO-CF and 1-BAGO-CF are termed 0.25-BAGO-CFRE, 0.5-BAGO-CFRE and 1-BAGO-CFRE respectively.

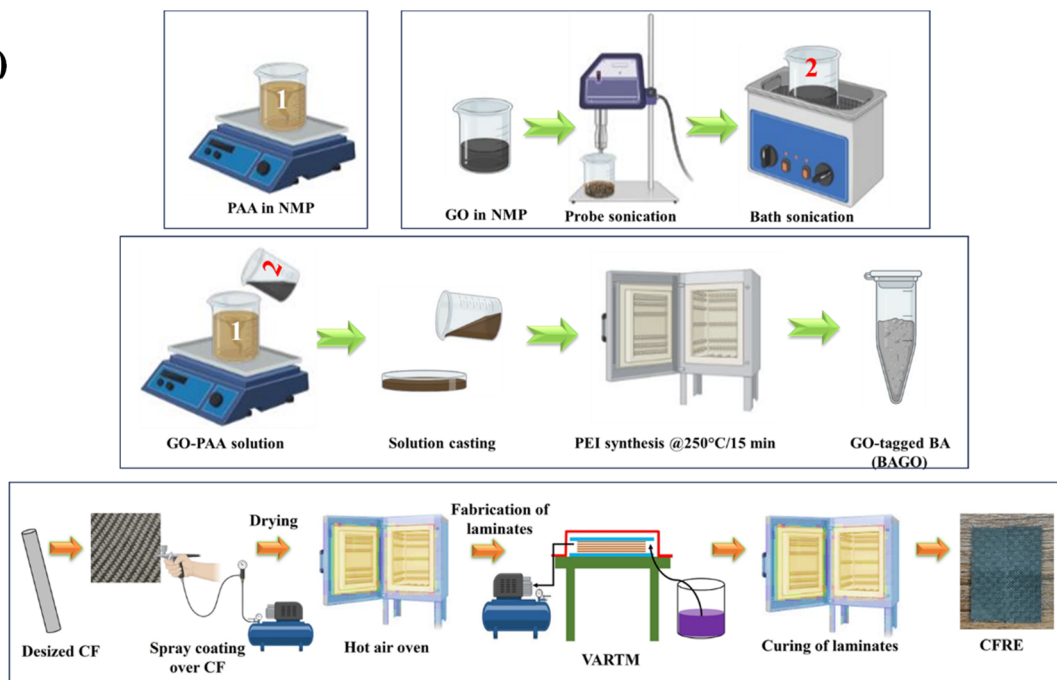
## 4. Characterization

### 4.1. Microstructural and surface characterization

The synthesized BA was validated by Fourier transform infrared (FTIR) spectroscopy performed on a PerkinElmer spectrometer (PES) in attenuated total reflectance (ATR) mode in the scanning range of 650–4000  $\text{cm}^{-1}$ . X-ray diffraction (XRD) was conducted on a Bruker D8 Advance instrument, employing a copper K $\alpha$  X-ray source with a wavelength ( $\lambda$ ) of 1.5406  $\text{\AA}$ . Raman spectral data were obtained with WITec system equipment with an excitation wavelength of 532 nm. The structural homogeneity of the sample was determined by measuring the intensity ratio of peaks at 1350  $\text{cm}^{-1}$  (D band) and 1582  $\text{cm}^{-1}$  (G band). Thermogravimetric analysis (TGA) was performed to investigate the thermal stability of BA and BAGO using a TA Instruments Q500 instrument. The analysis was conducted over a temperature range of 40  $^{\circ}\text{C}$  to 600  $^{\circ}\text{C}$ , with a heating rate of 10  $^{\circ}\text{C}$  per minute. The structure morphology of GO and BAGO was analyzed using a Zeiss Ultra FESEM (Field Emission Scanning Electron Microscope) operating at an accelerating voltage of 5 kV. The surface morphology of CF-mats before and after sizing agent deposition was carried out using FESEM. Surface roughness analysis of both pristine and modified CFs was conducted using an atomic force microscope (AFM) in noncontact mode. The CFs were securely stretched and pinned to support, and the examination was carried out using a PARK NX-10 microscope. The measuring surface area was 10  $\times$  10  $\mu\text{m}^2$ , featuring 2  $\mu\text{m}$  vertical corrugations, and was made possible using a cylindrical piezo transducer. To investigate the wetting behavior, a Kyowa contact angle goniometer was employed to measure the contact angle of both pristine and modified CFs. Additionally, surface-free energy studies assessed epoxy's compatibility with modified CFs. In this study, the solvents employed were deionized (DI) water and ethylene glycol. The Owens, Wendt, Rabel, and Kaelble (OWRK) method was utilized to compute the CFs' dispersive and polar components and overall surface-free energy.<sup>38</sup>

To assess the electromagnetic interference (EMI) shielding performance, a Keysight Field Fox microwave analyzer, model N9918A, operating within the frequency range of 12.4 to 18 GHz K $_{\text{u}}$  band was employed. The sample thickness was 2.2 to 2.4 mm. The EMI shielding efficiency (EMI SE) of a material is expressed in terms of its ability to attenuate the incoming EM wave on the shield through *R*, *A* and *M*, where *R* refers to the reflectivity or reflection coefficient, *A* refers to the absorption coefficient or absorptivity and *M* refers to multiple internal reflections. The term “transmission coefficient” or “transmis-

(a)



(b)

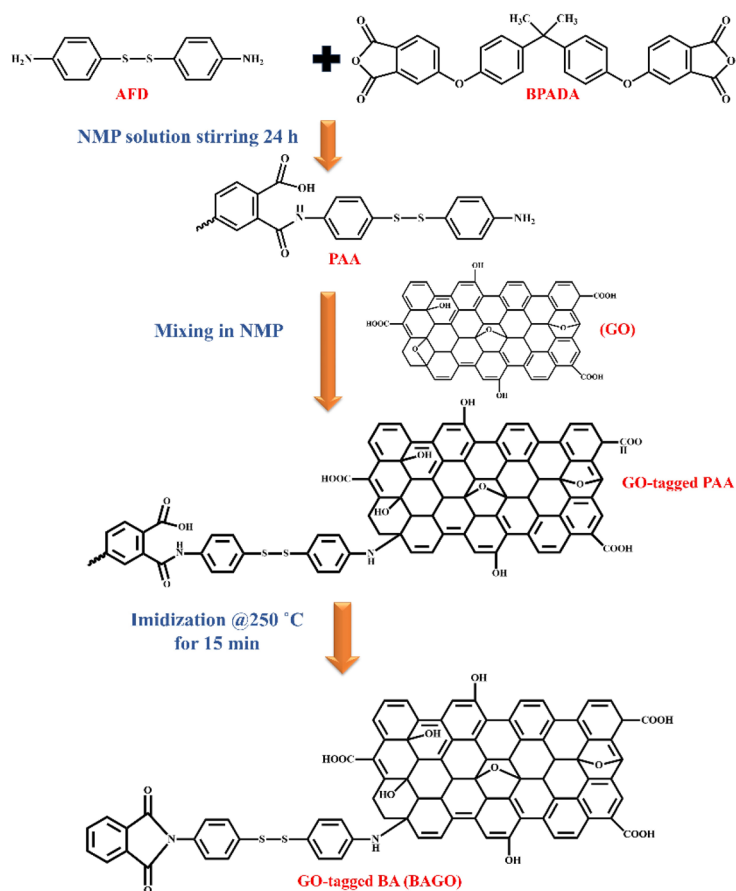


Fig. 1 (a) Schematic of the synthesis of BAGO and fabrication of modified CFRE, and the (b) reaction scheme of BAGO.

sivity  $T$  refers to the portion of the incident electromagnetic wave that is reflected from the surface of the electromagnetic shields but does not pass through the shield. On the other hand, the portion of the wave that is not reflected and passes through the shield is still transmitted. It is possible to absorb, disperse, or convert the electromagnetic energy linked to the portion of the incident electromagnetic waves that are passing through the shield material to heat. Another element that is taken into account as a correction term for thin shields in media with finite dimensions is  $M$ . The overall contributions of these three factors result in the total EMI SE ( $SE_T$ ) which is calculated using the following equation:

$$SE_T = SE_R + SE_A + SE_M \quad (1)$$

where  $SE_A$ ,  $SE_R$ , and  $SE_M$  denote shielding *via* absorption, reflection, and multiple reflections, respectively.  $SE_M$  can be overlooked when  $SE_T > 15$  dB or when the shield thickness exceeds the skin depth.<sup>39</sup> In a vector network analyzer, EMI SE is represented in terms of scattering parameters which are  $S_{11}$  (forward reflection coefficient),  $S_{12}$  (forward transmission coefficient),  $S_{21}$  (backward transmission coefficient), and  $S_{22}$  (reverse reflection coefficient). The  $SE_T$  can be calculated from the  $S$  parameters by using some equations as discussed in the ESI.<sup>†</sup> The detailed theory of EMI shielding is presented in section S5 of the ESI.<sup>†</sup>

The electrothermal property was evaluated by applying an external voltage to the sample. DC power supply with 60 volts and 10 amperes specifications. The sample was fixed with copper clips connected to the DC power supply. The sample edges were gently polished to reveal the surface of CF, and copper strips were connected to the ends to ensure optimal contact between the electrode and the sample. The separation distance between the electrodes was set at 15 mm. A constant input of 8 volts (3.52 watts) was externally supplied to the sample, and temperature measurements were carried out using an infrared thermal imaging system. An experiment for measuring deicing was conducted at constant applied voltage (8V) which generates Joule heating.

## 4.2. Mechanical properties

The ILSS and FS tests for both the pristine and modified laminates were conducted according to standards ASTM D7264 and ASTM D2344, respectively. A ZwickRoell Universal Testing Machine (UTM) with a 5 kN load cell was employed for these tests, maintaining a loading rate of 1 mm per minute. For each testing condition, six samples were tested, and the reported results include the average value, standard deviation (SD), and coefficient of variance (COV).

FS was calculated using eqn (2):

$$\sigma = \frac{3Pl}{2bh^2} \quad (2)$$

and ILSS was calculated using eqn (3):

$$\sigma = \frac{3P}{4bh} \quad (3)$$

where  $P$  represents the applied load.  $b$  denotes the width of the sample.  $h$  represents the depth of the sample.  $l$  represents the gauge length of the sample.

The ILSS test was terminated manually after the load had declined to 30% of the peak load, as per the ASTM D2344 standard. Subsequently, the ILSS-tested samples were unloaded and heated at 200 °C for 15 minutes in an oven and then slowly cooled down to room temperature for self-healing and retested for ILSS to determine the effect of self-healing. Another set of ILSS tested virgin samples were retested for ILSS without any self-healing to determine the residual strength. The self-healing efficiency was calculated by using eqn (4),<sup>40</sup>

$$\%SH = \frac{P_{SH} - P_{RS}}{P_V - P_{RS}} \times 100 \quad (4)$$

where  $P_{SH}$  represents the peak load of the sample retested after self-healing.  $P_{RS}$  represents the peak load of the sample retested without any self-healing.  $P_V$  represents the peak load of the virgin (original, untested) sample.

A scanning acoustic microscope (SAM) was used to observe the effect of self-healing. Here, we have used a 3D scan to observe the image of the virgin sample and the ILSS tested virgin samples before and after self-healing. This test was conducted using a KSI GERMANY 400 with a 50 MHz transducer and 4000 resolutions. The sample depth was ~2.4 mm.

## 4.3. Fractography

Fractographic analysis of the fractured flexural test samples was conducted using a Zeiss Ultra FESEM (Field Emission Scanning Electron Microscope) with an accelerating voltage of 5 kV. The cross-sectional examination of the fractured samples aimed to gain insights into the impact of sizing materials on CF surface modification and its influence on the interface of CFRE laminates.

# 5. Results and discussion

## 5.1. FTIR of BA and BAGO

Fig. 2a presents the FTIR spectra of BA and BAGO. BA exhibits imide and carbonyl stretching frequencies at 1716  $\text{cm}^{-1}$  and 1775  $\text{cm}^{-1}$ . The imide formation happened due to the reaction between BPADA and AFD.<sup>41</sup> The presence of aliphatic and aromatic C-H stretching frequency in BA was observed in the range of 2900–3100  $\text{cm}^{-1}$ . The characteristic peaks at 663  $\text{cm}^{-1}$  and 1476  $\text{cm}^{-1}$ , indicative of C-S bonds, are observed in BA.<sup>42</sup> However, from Fig. S1,<sup>†</sup> the peak observed at 3196  $\text{cm}^{-1}$  in the high-frequency zone is identified as the stretching bond of O-H, signifying the presence of O-H functional groups in GO. The band observed at 1716  $\text{cm}^{-1}$  is attributed to the carboxyl group. The sharp peak identified at 1615  $\text{cm}^{-1}$  can be attributed to the C=C bond. The peak at 1044  $\text{cm}^{-1}$  represents the vibrational mode of C-O-H. In this case, from Fig. S1,<sup>†</sup> we observe a prominent signal at 1228  $\text{cm}^{-1}$ , which corresponds to the stretching vibration of the epoxy (C-O) group.

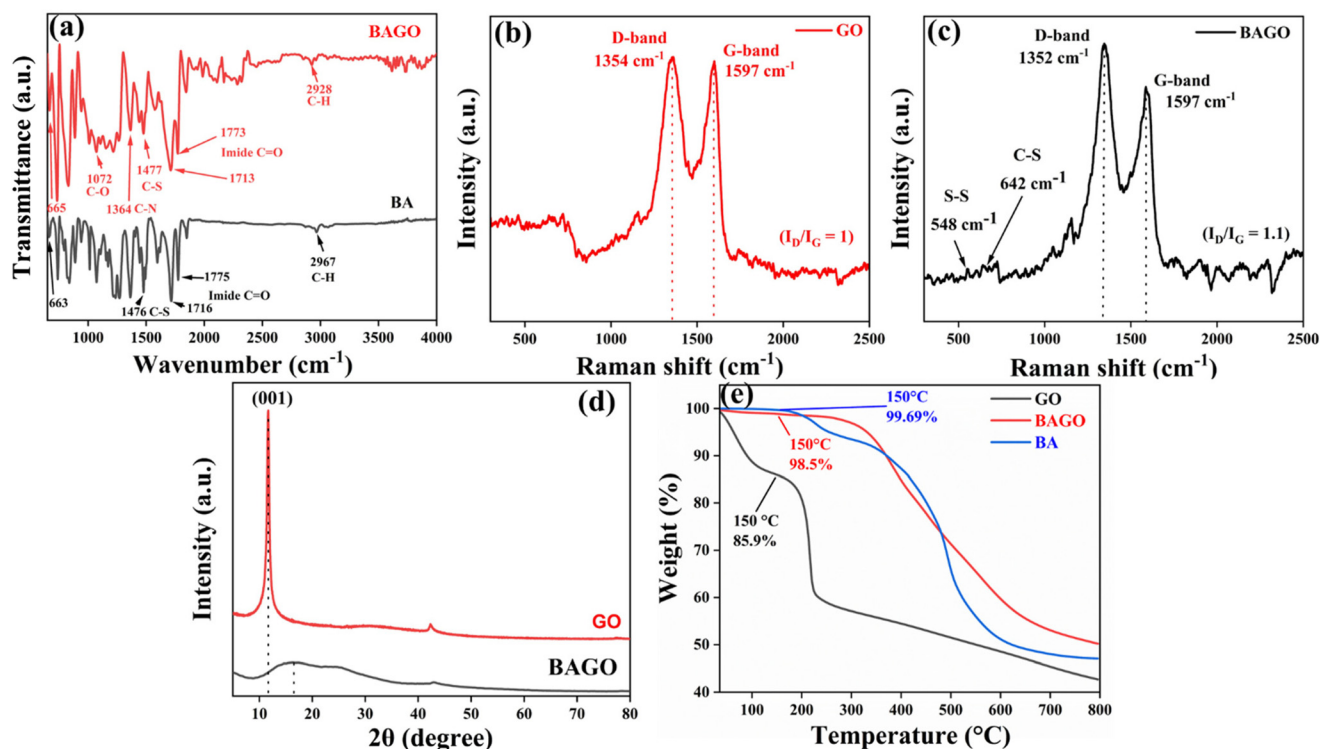


Fig. 2 (a) FTIR spectra of BA and BAGO, (b) Raman spectra of GO, (c) Raman spectra of BAGO, (d) XRD of BA and BAGO and (e) TGA of GO, BA and BAGO.

Additionally, another distinct peak at  $988\text{ cm}^{-1}$  can be attributed to the presence of peroxide or epoxy functional groups within GO.<sup>43</sup> In the case of BAGO, all the characteristic peaks present in BA and GO are retained. However, during the synthesis of BAGO, the reduction of GO occurs resulting in the disappearance of a broad peak at around  $3000\text{--}3400\text{ cm}^{-1}$  associated with the hydroxyl group due to deoxygenation. This phenomenon explains the absence of hydroxyl peaks in BAGO (Fig. 2a). Furthermore, the epoxy peaks, which are evident in GO, are notably absent in BAGO. This absence could potentially be attributed to a reaction occurring during the mixing and imidization processes, wherein certain amines from PAA interact with the epoxy groups on GO,<sup>44</sup> as depicted in the scheme shown in Fig. 1b. This observation provides supporting evidence for the GO being tagged to BA. Fig. S2† demonstrates the elemental analysis of GO and BAGO.

## 5.2. Raman spectra of GO and BAGO

The Raman spectra of GO and BAGO are illustrated in Fig. 2b and c. The D band observed at  $1354\text{ cm}^{-1}$  corresponds to surface defects, and the G band at  $1597\text{ cm}^{-1}$  corresponds to the graphitic structure of GO, respectively. However, after the incorporation of GO in BA, the positions of the D band are at  $1352\text{ cm}^{-1}$  and the G bands at  $1597\text{ cm}^{-1}$ , respectively. However, during the thermal imidization process, a thermal reduction of GO takes place resulting in an increase in the  $I_D/I_G$  ratio from 1 to 1.1, and a higher intensity ratio of the D

band to the G band ( $I_D/I_G$ ) in comparison to that found for GO indicates that the loss of the aromatic structure and the formation of new defects enhance the  $\text{sp}^3$  domain in the graphite layer.<sup>45</sup> By analyzing the Raman spectra of both GO and reduced-GO (rGO), we can predict that GO has undergone a reduction to become rGO. This prediction is based on the observed increase in the intensity ratio  $I_D/I_G$ , which indicates the integrated degree of disorder associated with the reduction process. Raman spectrum also demonstrates the existence of S-S and C-S bonds at  $548\text{ cm}^{-1}$  and  $642\text{ cm}^{-1}$ , respectively.

## 5.3. XRD of GO and BAGO

XRD patterns of GO and BAGO depicted in Fig. 2d show a sharp diffraction peak at  $11.64^\circ$  corresponding to the (001) planes of GO with a  $d$ -spacing of  $0.76\text{ nm}$ .<sup>46,47</sup> However, during the synthesis of BAGO, the thermal reduction of GO occurs and the (001) peak disappears. Instead, an amorphous hump is observed at  $16.52^\circ$ , which is attributed to amorphous BA.<sup>48,49</sup>

## 5.4. TGA of GO, BA and BAGO

The thermal stabilities of GO, BA and BAGO are illustrated in Fig. 2e. The initial decomposition of BA commences at around  $350^\circ\text{C}$ , triggered by the rupture of the C-S bond, leading to the release of sulfur.<sup>41,50</sup> Hence, the existence of the dynamic disulfide bond in BA imparts reduced thermal stability, resulting in a decrease in weight percentage.<sup>51</sup> However, after the

incorporation of GO, the thermal stability of BAGO is enhanced.<sup>52</sup> The weight loss observed at around 150 °C in GO is also not observed in BAGO due to the removal of the absorbed moisture and labile oxygen functional groups of GO during the processing of BAGO.<sup>51,53,81</sup>

### 5.5. Microstructure and morphology of neat CF and BAGO–CF

The surface characteristics of neat (desized) CF and BAGO sized CFs are shown in Fig. 3a and b. The neat fibers exhibit a rough surface with numerous longitudinal grooves (Fig. 3a). However, a uniform deposition of corrugated 0.25-BAGO (Fig. S3b†) on CF creates new grooves and ridges and increases the surface roughness of 0.25-BAGO–CF (Fig. 3b). However, at a higher content of GO, surface roughness reduces because agglomerated GO covers the surface grooves and ridges, as shown in Fig. S4.†

AFM images of neat CF and 0.25-BAGO–CF are shown in Fig. 3. The neat desized CFs exhibit a smooth surface with a surface roughness ( $R_a$ ) of 15 nm, as shown in Fig. 3c. The  $R_a$  value of 0.25-BAGO–CF is significantly enhanced to 140 nm, as shown in Fig. 3d, because it has created new undulation on surfaces. This more uneven surface will lead to better adhesion of CF with the epoxy matrix.<sup>54,55</sup>

### 5.6. Contact angle and surface energy of CFs

The wettability of neat (desized) CF and BAGO–CF was evaluated by measuring their contact angles with water (Fig. 4a) and ethylene glycol (Fig. S5†). The water contact angle of neat CF indicates its hydrophobic nature, as the contact angle is more than 90°. Following the modification with BAGO, the surface of the CF underwent a physicochemical transformation leading to a reduction in their water contact angle ( $\theta_{\text{water}}$ ) from 102.3° to 77°. Similarly, ethylene glycol contact angle ( $\theta_{\text{ethylene glycol}}$ ) decreased from 87.2° to 46°. The total surface energy of

that is the combination of dispersive ( $\gamma^d$ ) and polar ( $\gamma^p$ ) components is indirectly calculated from contact angle analysis.<sup>56</sup> Wettability of epoxy with CFs improves when the surface energy difference between epoxy and CF decreases.<sup>57,58</sup> The surface energy of epoxy is 33.5 mN m<sup>-1</sup>. Consequently, the deposition of 0.25-BAGO increases the surface energy to 34.7 mN m<sup>-1</sup> from 13.2 mN m<sup>-1</sup> of neat CF (Fig. 4b). Both the polar and dispersive components of surface energy increase. The polar component originates from the coulombic interactions involving the permanent or induced dipole components of polar functional groups while the dispersive component relates to van der Waals interactions among hydrocarbon chains.<sup>56</sup> The possible reason for the increase in surface energy is the increase in surface roughness (Fig. 3d) and the introduction of new functional groups. A higher loading of GO in BA leads to agglomeration lowering the surface energy.<sup>59</sup>

### 5.7. Mechanical properties of laminates

We have examined the effect of BA alone on mechanical properties. The amount of BA was optimized at 0.25 wt% of CF and the resulting laminate was termed BA–CFRE-0.25. For comparison those results are presented here as well, but for the sake of brevity, it is referred to as BA–CFRE here. For BAGO sizing of CF reported in the present manuscript, the amount of BAGO is kept the same as BA, *i.e.*, 0.25 wt% CF and the resulting laminate is referred to as BAGO–CFRE. Depending on the amount of GO in terms of wt% of BA, the three laminates are referred to as 0.25-BAGO–CFRE, 0.5-BAGO–CFRE and 1-BAGO–CFRE. The FS and ILSS evaluations provide insights into the structural properties of the laminates when subjected to complex stress conditions, encompassing both bending and shearing stresses.<sup>60</sup>

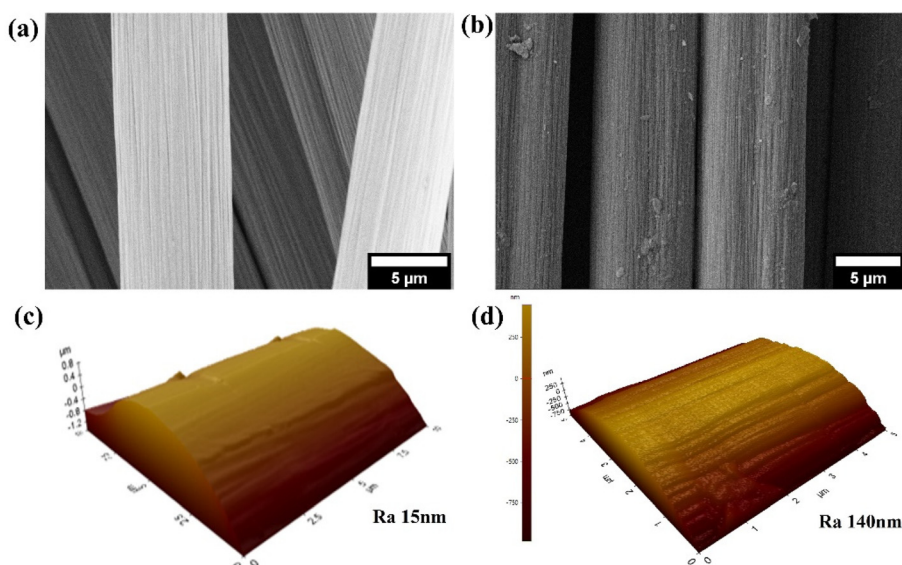


Fig. 3 SEM micrographs of (a) neat CF and (b) 0.25-BAGO–CF, and AFM images of (c) neat CF and (d) 0.25-BAGO–CF.

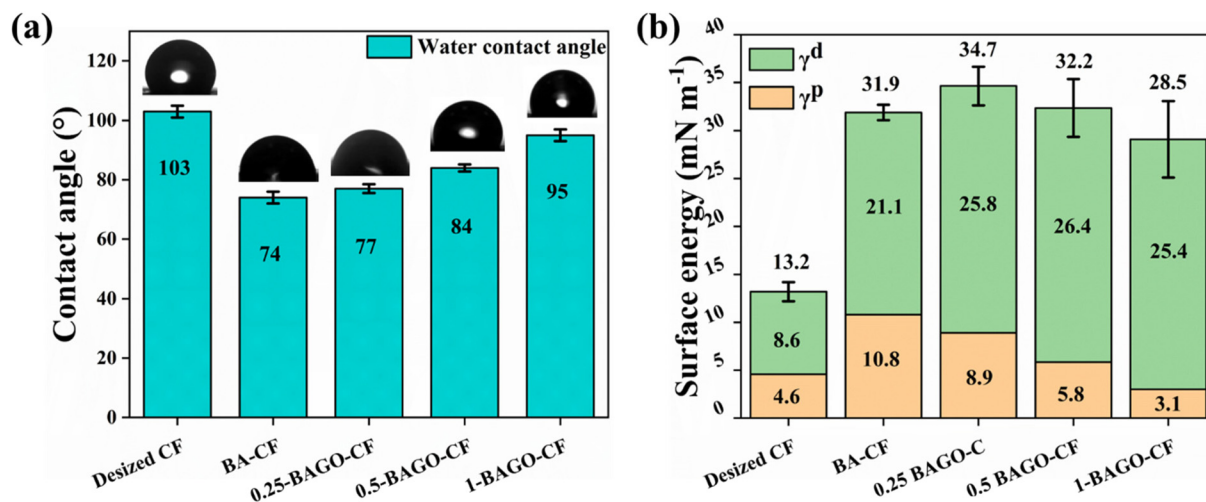


Fig. 4 (a) Water contact angle and (b) surface energy of desized and BAGO-CF.

**5.7.1. Flexural strength (FS).** Load-displacement curves for FS tests of neat CFRE, BA-CFRE and various BAGO-CFREs are shown in Fig. 5a and FS values derived from them are presented in Fig. 5b. BA-CFRE shows an FS value of 689 ( $\pm 6$ , COV 1.9) MPa with 19% improvement and GO-CFRE showed 15% improvement in FS in our previous work,<sup>26</sup> but the combined sizing of BA and GO in the present work, *i.e.*, 0.25-BAGO-CFRE gives an FS value of 808 MPa ( $\pm 41$ , COV 5), a substantial 40% enhancement over neat CFRE. The reason behind this exceptional improvement in FS is the strong interfacial interactions and bonding by BAGO. Furthermore, the wrinkled surface of GO contributes to increased surface roughness providing better adhesion with epoxy. Higher loading of GO in BA (0.5 and 1 wt%) reduces FS as compared to 0.25 wt% BAGO and results in 28% and 29% increase in FS, respectively, over neat CFRE, because excess GO agglomerated on the surface of CFs and reduced the interfacial strength between CFs and epoxy (Fig. S4†).

**5.7.2. Interlaminar shear strength (ILSS).** Load-displacement curves for ILSS tests of neat CFRE, BA-CFRE and various BAGO-CFREs are shown in Fig. 5c and ILSS values derived from them are presented in Fig. 5d. BA-CFRE shows an ILSS value of 58 ( $\pm 0.3$ , COV 1.14) MPa with a 26% increase and GO-CFRE showed an 18% increase in ILSS,<sup>26</sup> but the combined sizing of BA and GO in the present work, *i.e.*, 0.25-BAGO-CFRE gives an ILSS value of 62 ( $\pm 2.15$ , COV 3.5) MPa, a significant 35% increase over neat CFRE. Higher loading of GO in BA (0.5 and 1 wt%) reduces ILSS as compared to 0.25 wt% BAGO over neat CFRE due to agglomeration. However, we have fabricated 0.125-BAGO-CFRE as well, but it did not show exceptional results and we have seen a greater strength for 0.25-BAGO-CFRE. Thus, the trends for ILSS are the same as those for FS and the explanations given above for FS hold for ILSS as well.

Fig. 5e shows the comparison of ILSS values obtained with the BAGO sizing agent used in the present work with the ILSS values obtained by using various other sizing agents reported

in the literature.<sup>26,61–63</sup> As can be seen, the present work has yielded higher values for 0.25-BAGO-CFRE laminates.

## 5.8. Self-healing

Many authors have calculated self-healing efficiency in the literature by using the following equation:<sup>40,64–66</sup>

$$\%SH = (P_{SH}/P_V) \times 100 \quad (5)$$

where  $P_{SH}$  and  $P_V$  have been defined in eqn (4). We have already pointed out the fallacy in this definition in our previous paper because it does not take into account the residual strength of the virgin sample after the ILSS test. Therefore, we have used eqn (4) for calculating self-healing efficiency proposed by Nassho *et al.*<sup>40</sup> Fig. 6a shows the load-displacement curves for the virgin 0.25-BAGO-CFRE sample and retested samples without self-healing and after self-healing, and Fig. 6b shows the ILSS values of the virgin sample and self-healed sample. The values of  $P_{SH}$ ,  $P_{RS}$  and  $P_V$  obtained from Fig. 6a are 1739 N, 1433 N and 2039 N, respectively, and self-healing efficiency is obtained from eqn (4) as 51%. It is slightly higher than that for BA-CFRE (50%) (Fig. S6†). The self-healing mechanism in BAGO-sized laminates is attributed to the dynamic disulfide (S–S) metathesis facilitated by associative CAN. When subjected to the ILSS test, these bonds break under mechanical stress and reassemble through disulfide metathesis on self-healing.

## 5.9. SAM

In this study, we have employed a scanning acoustic microscope for the first time to investigate the healing process in CFRE laminates. This powerful, non-destructive technique allows for examining the overall microstructure of CFRE laminates.<sup>67,68</sup> The non-destructive nature of high-resolution ultrasonic vision makes it an exceptional tool for exploring the actual mechanisms underlying the failure of CFRE laminates.

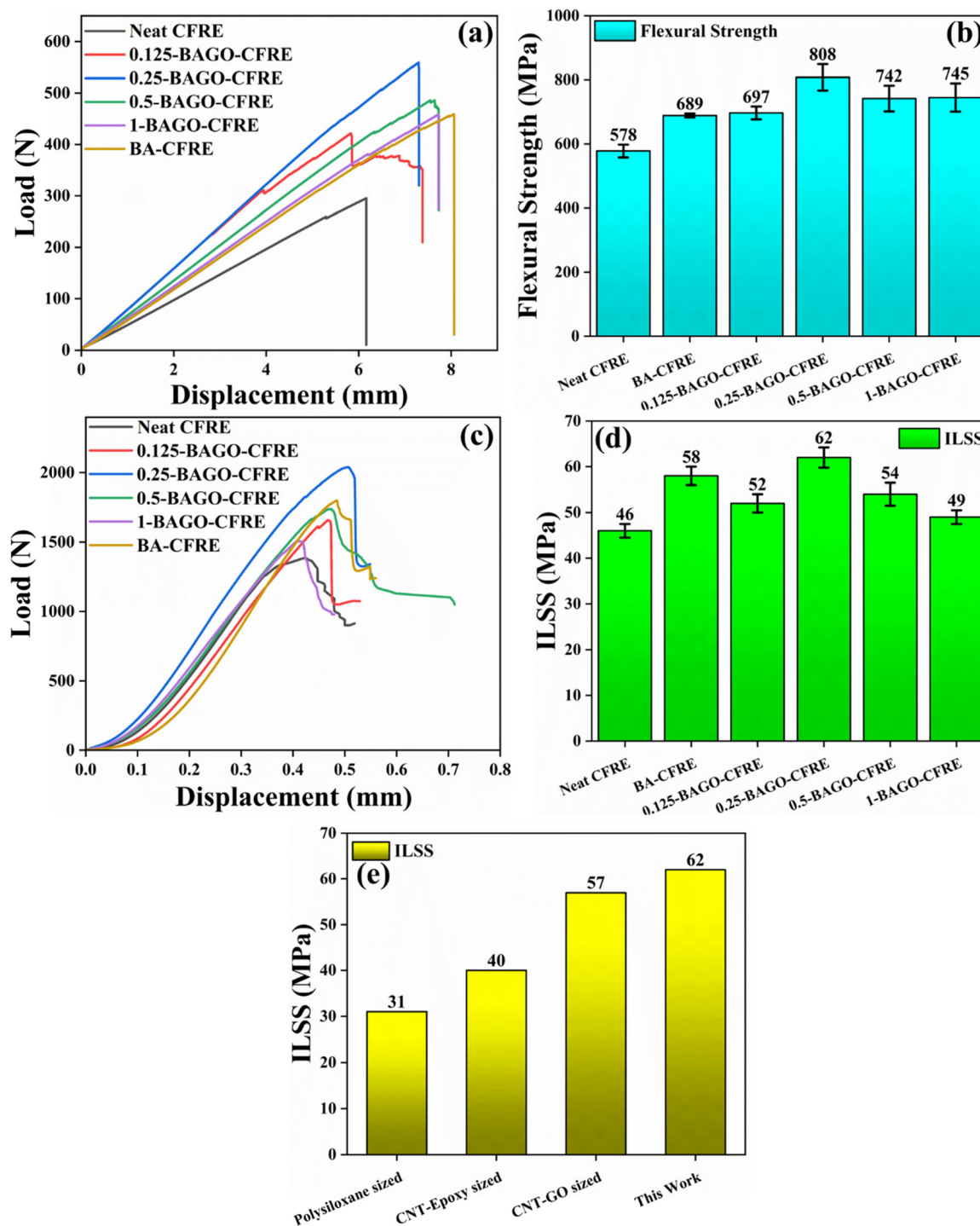


**Fig. 5** (a) Load vs. displacement curve of flexural strength, (b) flexural strength of neat and BAGO-CFRE, (c) load vs. displacement curve of ILSS, (d) ILSS of neat and BAGO-CFRE, and (e) ILSS comparison of the literature with present work.

This tool effectively reveals and characterizes CFRE laminates with micrometer level resolution before and after self-healing treatment, as shown in Fig. 6c. In the case of neat CFRE, the CF mat is clearly visible. However, following the ILSS test, the central portion is blurred indicating fiber damage. Remarkably, after the self-healing treatment, the blurring has drastically reduced indicating the recovery of the laminate.

#### 5.10. Interfacial strengthening and self-healing mechanisms

Based on the preceding discussion, it is evident that incorporating the BA sizing agent enhances surface roughness, fosters secondary interactions with epoxy, and improves wettability. These enhancements contribute to increased interfacial adhesion, which, in turn, manifests in improved mechanical

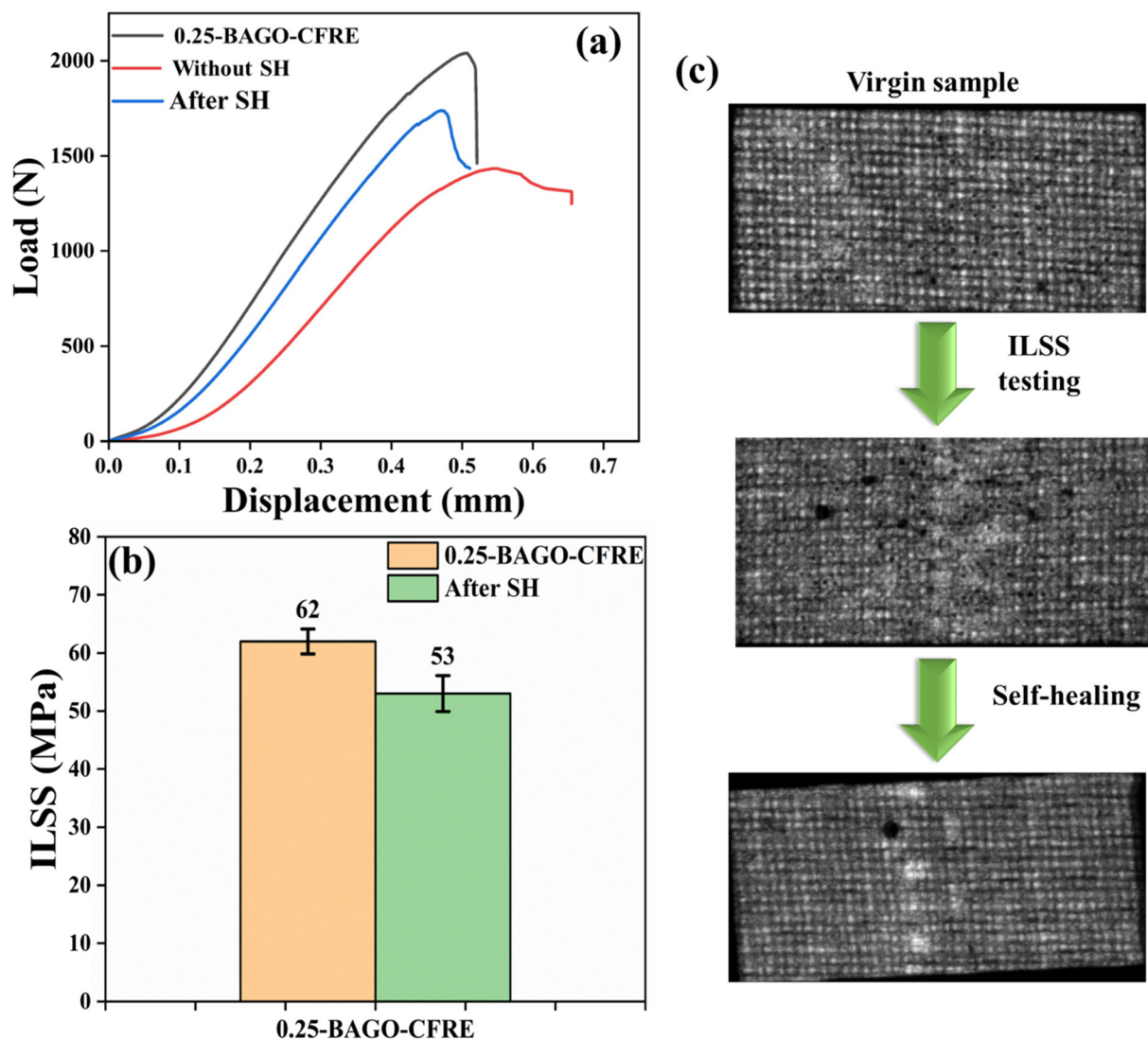


**Fig. 6** (a) and (b) Load vs. displacement curve bar graph of self-healing of 0.25-BAGO-CFRE, and (c) SAM micrograph of before and after self-healing graph.

properties (Fig. 5(a–d)). Furthermore, tagging of GO with the BA sizing agent amplifies the surface roughness owing to its characteristic wrinkled morphology, thus lowering the contact angle increases the surface energy. GO also introduces new functional groups to the sizing agent. Consequently, this BAGO sizing agent-modified carbon fibers engage in more profound chemical interactions (such as polar interactions, pi-pi interactions, H-bonding, or even the formation of covalent bonds) with the epoxy depicted in Fig. 7a. These interactions reinforce the interface and increase ILSS and FS (Fig. 5a–d). However, at higher loadings of GO in the BAGO sizing agent, the GO sheets can agglomerate reducing the interfacial strength (Fig. S4† and Fig. 5d).

The self-healing mechanism employed by BAGO relies on the disulfide metathesis reaction illustrated in Fig. 7b. The mechanism of disulfide metathesis is well established in the literature.<sup>69,70</sup> We selected a self-healing condition of 200 °C

for 15 minutes. This choice aligns with the fact that the glass transition temperature  $T_g$  of this CFRE is 180 °C. Beyond  $T_g$ , molecular segmental motion becomes more pronounced, allowing the bonds to draw nearer to each other and thereby facilitating the exchange reaction.<sup>71,72</sup> The S–S bond in the primary backbone chain undergoes dissociation during the ILSS test and subsequently recombines after the sample is subjected to a self-heat treatment. This process results in the restoration of interfaces and ILSS.

### 5.11. Fractography

The fracture surfaces of neat and 0.25-BAGO-CFRE after the flexural test are shown in Fig. 8a and b. Here, we can see that the epoxy on the neat sample experienced complete detachment from the fiber surface. As a result, fiber debonding takes place with fiber pulling out and leaving the voids in the matrix. This can be ascribed to inadequate adhesion, which is

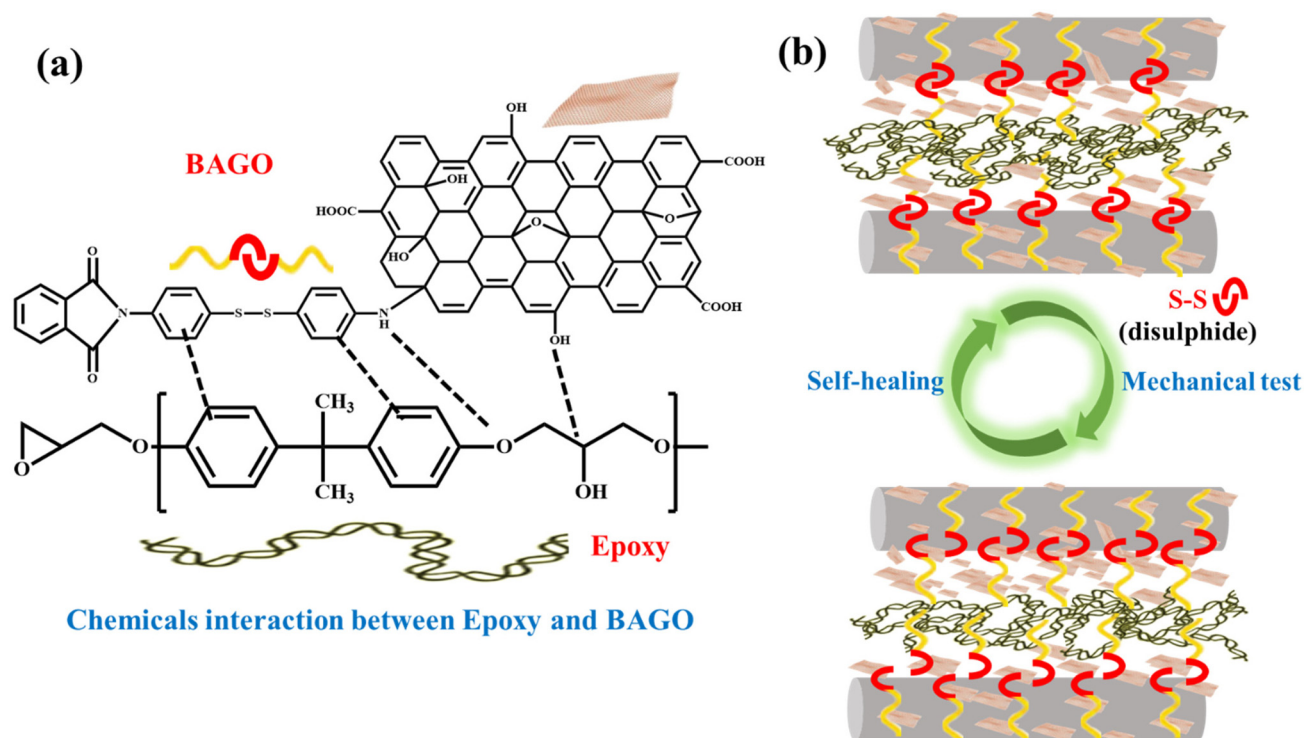


Fig. 7 (a) Interaction between the sizing agent and the epoxy and (b) schematic of self-healing mechanisms.

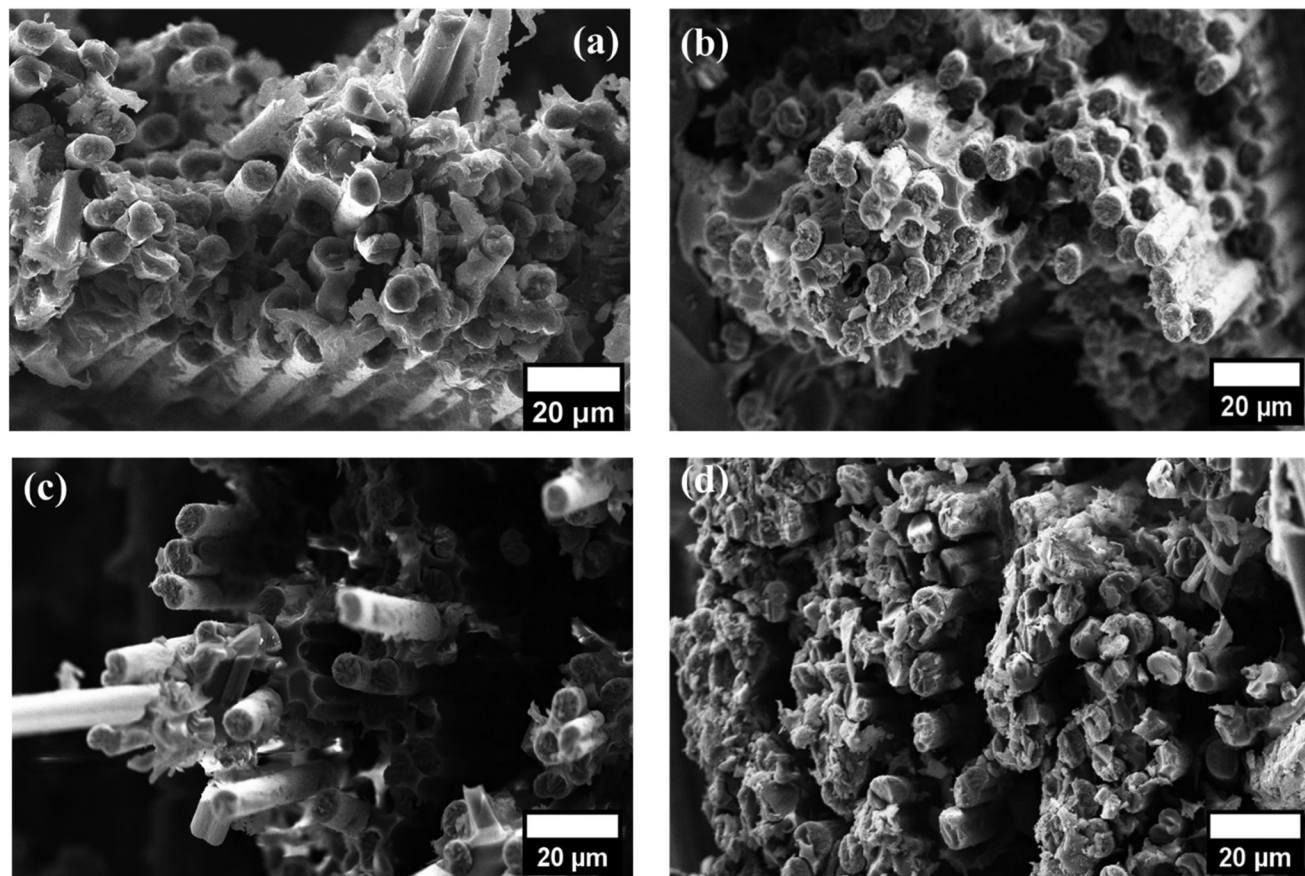


Fig. 8 Fractography images of FS tested samples: (a) neat, (b) 0.25-BAGO-CFRE, (c) 0.5-BAGO-CFRE, and (d) 1-BAGO-CFRE.

predominant in interface-related failure. In contrast, epoxy is observed to adhere at the fiber surface for 0.25-BAGO-CFRE in Fig. 8b. This observation indicates that the interfacial adhesion between the fibers and epoxy is enhanced by sizing 0.25-BAGO onto the fiber surface. The improvement can be ascribed to the interlocking effect and chemical bonds between 0.25-BAGO-CF and epoxy. However, a higher loading of GO in the sizing agent reduced the adhesion between the fiber and matrix due to the agglomeration of GO, which reduces surface roughness and hinders the resin from effectively wetting the fibers (Fig. 8c and d).

### 5.12. Thermal imaging (Joule heating) and deicing

Accumulation of ice on aircraft wings can have severe consequences, including the potential for fatal failures including sensor and equipment malfunctions. The additional weight on the wing's surface can disrupt the aircraft's aerodynamics, resulting in decreased lift and increased drag, ultimately causing higher fuel consumption. Addressing these issues with laminates containing 0.25-BAGO-CF could widen its utility in aerospace applications.

Fig. 9a demonstrates the temperature profile along with the IR thermal images of the neat CFRE and while applying a constant voltage of 8 V for 300 s and then switching it off (Fig. 9b). The temperature reached up to 76 °C for neat CFRE, whereas it reached 142 °C for the 0.25-BAGO-CFRE sample. The higher temperature rise for 0.25-BAGO-CFRE is attributed to the greater Joule heating.<sup>73,74</sup> As we can see in Fig. S7,<sup>†</sup> the surface electrical conductivity of 0.25-BAGO-CFRE is higher compared to neat CFRE. As shown earlier, during the synthesis of BAGO, partial reduction of GO occurred and reduced GO has very high electrical conductivity.<sup>75,76</sup> Therefore, the presence of conducting BAGO over CFs in 0.25-BAGO-CFRE increases the electrical conductivity and results in higher Joule heating observed (Fig. 9b) as compared to neat CFRE.<sup>26,77</sup>

The deicing capabilities of the 0.25-BAGO-CFRE system were demonstrated by placing ~50 mg ice on the sample's surface and applying Joule heating at 8 V for ~1 min. As depicted in Fig. 9c, the ice begins to melt within 30 s, and is completely melted in 50 s, whereas these times were 35 s and 65 s for neat CFRE. These results clearly show the remarkable electrothermal heating and deicing performance of the 0.25-BAGO-CFRE nanocomposite.

### 5.13. EMI shielding performance

CFRE laminates integrated with excellent EMI shielding capability are highly desired on account of their extensive applicability in aerospace applications. To prevent interference in the smooth operation of regular communication systems, disturbance in broadcasting signals, and information leakage, the development of radar-absorbing materials (RAMs) is in high demand.<sup>26</sup>

We have assessed the EMI SE of our prepared self-healable CFRE laminates introducing our novel sizing agent GO-tagged PEI along with the control sample in three distinct frequency bands *i.e.*,  $K_u$  in a frequency regime of 12.4–18 GHz. The total EMI shielding efficiency ( $SE_T$ ) vs. frequency of the CFRE laminates (average thickness 2.2–2.4 mm) with varying contents of the sizing agent are shown in Fig. 10a. It is evident that neat CFRE laminate without the sizing agent showed −47 dB in the  $K_u$  band. The laminates modified with BAGO were also observed in a similar range indicating that the coating of an additional layer (here BAGO) did not alter (rather sacrifice) the shielding capability of the laminates. A minor increase in the surface conductivity which resulted in improved deicing performance did not yield significant changes in EMI SE. The inherent improvement in SE in CFRE laminates is due to multiple reflections between and within the conductive fibers.<sup>78,83</sup> In contrast, the incorporation of the sizing agent may lead to impediment in charge transport thereby reducing the EMI

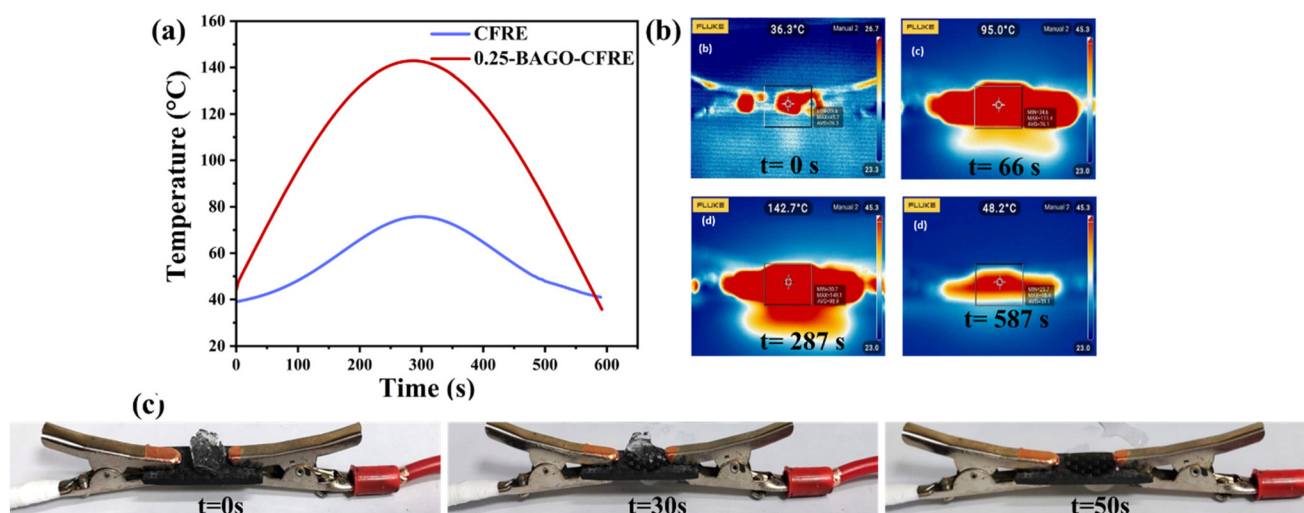


Fig. 9 (a) Temperature vs. time graph at 8 V, (b) infrared thermal image of 0.25-BAGO-CFRE subjected to Joule heating, and (c) images of 0.25-BAGO-CFRE during deicing.

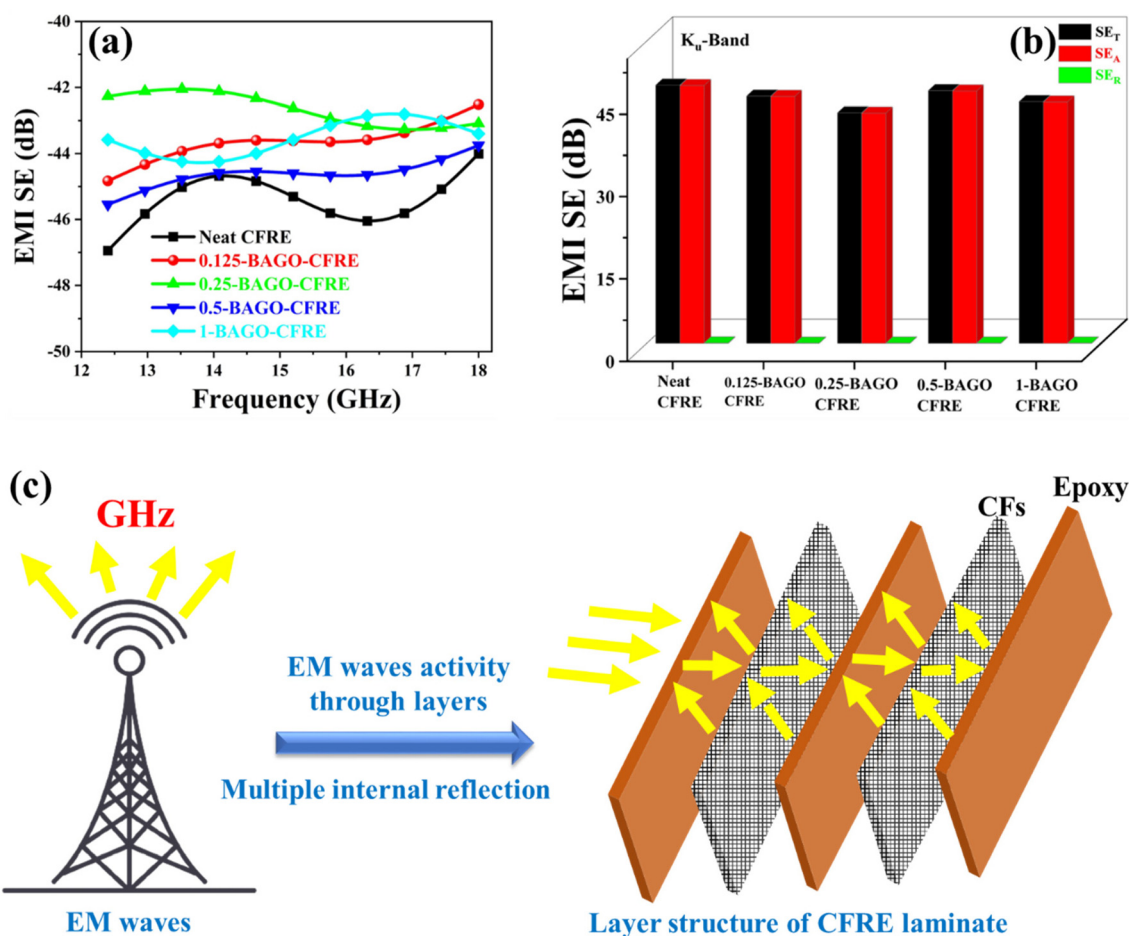


Fig. 10 (a) and (b)  $K_u$  band of neat and BAGO–CFRE and (c) schematic representation of EM wave activity through the CFRE layer.

SE.<sup>78</sup> As CFRE laminates are inherently conducting by virtue of the in-plane directional conductivity of the CF mat, the insertion of GO into the CFRE laminates was expected to enhance the conductivity of the composite. The bulk volume conductivity (not shown here) did not change due to the presence of BAGO, however, the surface conductivity increased marginally. As indicated earlier the partial reduction in GO (during the synthesis of BAGO) may have increased the resistivity in the thickness direction, however, this may improve in the in-plane direction.<sup>79</sup> Such observations are well correlated with the earlier reported works.<sup>79,80</sup> Taken together, a nonuniform conductive mesh between the epoxy and CF mat increases the SE as reported in our earlier work.<sup>39</sup>

The contributions to EMI SE from absorption ( $SE_A$ ) and reflections ( $SE_R$ ) components were also estimated from the measured  $S$  parameters using the equations discussed in the ESI† and are shown in Fig. 10b. The inferior microwave reflection and strong microwave absorption corresponding to the CFRE laminates with the varying concentration of the sizing agent indicate an absorption-based shielding mechanism. Such absorption-dominated shielding can be explained by the generation of heterogeneous interfaces at the junction of epoxy and CF mat in the fabricated CFRE laminates.<sup>39</sup>

Furthermore, the incorporation of BAGO as the sizing agent at the interface of CF and epoxy forms a nonuniform interfacial junction leading to interfacial polarizations and multiple internal reflections as schematically presented in Fig. 10c.

## 6. Conclusion

In this study, a unique sizing agent (here GO tagged PEI) with self-healing properties was designed to improve the interfacial strength in CFRE laminates. At a particular loading (here 0.25 wt% GO with respect to the sizing agent), a significant improvement in mechanical properties was observed. Our study has yielded some intriguing and noteworthy findings, as summarized below.

- The designer sizing agent (here BAGO) increases the surface roughness from 15 nm to 140 nm and the surface energy from 13 to 35 mN m<sup>-1</sup>.
- At a particular loading (here 0.25 wt% GO with respect to the sizing agent) the 26 modified CFRE showed an improvement in FS and ILSS by 40% and 35% respectively, as compared to neat CFRE.

• The enhanced mechanical properties can be attributed to the increase in surface roughness mimicking ‘Velcro-like structures’ resulting in mechanical interlocking of epoxy with the modified CF. This together with primary and secondary interactions between the BAGO-modified fibers and epoxy resulted in improved properties. However, beyond 0.25 wt% GO, poor dispersibility and non-uniform deposition were noted, potentially creating weak zones in CFRE and diminishing the mechanical properties.

• The ILSS tested sample 0.25-BAGO-CFRE shows self-healing with ~51% recovery due to the presence of dynamic disulfide bonds in BAGO.

• The modified CFRE laminates showed excellent Joule heating, deicing performance and EMI shielding properties.

## Conflicts of interest

There are no conflicts to declare.

## References

- 1 D. D. L. Chung, *Composite Materials*, Springer London, London, 2010.
- 2 R. Soni, R. Verma, R. Kumar Garg and V. Sharma, *Mater. Today: Proc.*, 2023, DOI: [10.1016/j.matpr.2023.08.108](https://doi.org/10.1016/j.matpr.2023.08.108).
- 3 A. Bisht, K. Dasgupta and D. Lahiri, *Composites, Part A*, 2019, **126**, 105601.
- 4 J. Seyyed Monfared Zanjani, B. Saner Okan, P.-N. Pappas, C. Galiotis, Y. Z. Menceloglu and M. Yildiz, *Composites, Part A*, 2018, **106**, 1–10.
- 5 H. Zhou, X. Du, H.-Y. Liu, H. Zhou, Y. Zhang and Y.-W. Mai, *Compos. Sci. Technol.*, 2017, **140**, 46–53.
- 6 X. Du, H. Zhou, W. Sun, H.-Y. Liu, G. Zhou, H. Zhou and Y.-W. Mai, *Compos. Sci. Technol.*, 2017, **140**, 123–133.
- 7 M. M. Rahman, S. Zainuddin, M. V. Hosur, J. E. Malone, M. B. A. Salam, A. Kumar and S. Jeelani, *Compos. Struct.*, 2012, **94**, 2397–2406.
- 8 Q. Song, K. Li, L. Qi, H. Li, J. Lu, L. Zhang and Q. Fu, *Mater. Sci. Eng., A*, 2013, **564**, 71–75.
- 9 E. Lee, C. Lee, Y.-S. Chun, C. Han and D.-S. Lim, *Composites, Part B*, 2017, **116**, 451–458.
- 10 J. Liu, Y. Tian, Y. Chen and J. Liang, *Appl. Surf. Sci.*, 2010, **256**, 6199–6204.
- 11 E. Hassan, T. Elagib, H. Memon, M. Yu and S. Zhu, *Materials*, 2019, **12**, 778.
- 12 M. A. Downey and L. T. Drzal, *Composites, Part A*, 2016, **90**, 687–698.
- 13 J. L. Thomason and L. J. Adzima, *Composites, Part A*, 2001, **32**, 313–321.
- 14 L. Ma, N. Li, G. Wu, G. Song, X. Li, P. Han, G. Wang and Y. Huang, *Appl. Surf. Sci.*, 2018, **433**, 560–567.
- 15 R. L. Zhang, Y. D. Huang, D. Su, L. Liu and Y. R. Tang, *Mater. Des.*, 2012, **34**, 649–654.
- 16 F. Zhao and Y. Huang, *J. Mater. Chem.*, 2011, **21**, 3695.
- 17 S. Deng, X. Zhou, C. Fan, Q. Lin and X. Zhou, *Composites, Part A*, 2012, **43**, 990–996.
- 18 Z. Liu, B. Song, T. Wang and L. Wang, *Appl. Surf. Sci.*, 2020, **512**, 145719.
- 19 F. Zhao and Y. Huang, *J. Mater. Chem.*, 2011, **21**, 3695.
- 20 S. G. Prolongo, B. G. Meliton, G. Del Rosario and A. Ureña, *Carbon*, 2012, **50**, 5489–5497.
- 21 J. M. Parente, R. Simões and P. N. B. Reis, *Procedia Struct. Integr.*, 2022, **37**, 820–825.
- 22 A. Yazdanfar and H. Shahrajabian, *Int. J. Adv. Manuf. Technol.*, 2021, **116**, 1801–1817.
- 23 Z. Guo, L. Song, C. G. Boay, Z. Li, Y. Li and Z. Wang, *Compos. Struct.*, 2018, **199**, 1–9.
- 24 W. Qin, F. Vautard, L. T. Drzal and J. Yu, *Composites, Part B*, 2015, **69**, 335–341.
- 25 X. Zhang and G. Wu, *Polymers*, 2018, **10**, 1171.
- 26 S. Parasuram, P. Banerjee, R. Raj, S. Kumar and S. Bose, *ACS Appl. Mater. Interfaces*, 2023, **15**, 28581–28593.
- 27 L. Vaisman, H. D. Wagner and G. Marom, *Adv. Colloid Interface Sci.*, 2006, **128–130**, 37–46.
- 28 A. C. Zaman, F. Kaya and C. Kaya, *Ceram. Int.*, 2020, **46**, 29120–29129.
- 29 A. E. Scott, M. Mavrogordato, P. Wright, I. Sinclair and S. M. Spearing, *Compos. Sci. Technol.*, 2011, **71**, 1471–1477.
- 30 S. R. White, N. R. Sottos, P. H. Geubelle, J. S. Moore, M. R. Kessler, S. R. Sriram, E. N. Brown and S. Viswanathan, *Nature*, 2001, **409**, 794–797.
- 31 M. R. Kessler, N. R. Sottos and S. R. White, *Composites, Part A*, 2003, **34**, 743–753.
- 32 R. Esmaeely Neisiany, J. K. Y. Lee, S. Nouri Khorasani, R. Bagheri and S. Ramakrishna, *J. Ind. Eng. Chem.*, 2018, **59**, 456–466.
- 33 X. Wu, A. Rahman, Z. Zhou, D. D. Pelot, S. Sinha-Ray, B. Chen, S. Payne and A. L. Yarin, *J. Appl. Polym. Sci.*, 2013, **129**, 1383–1393.
- 34 W. Zhang, J. Duchet and J. F. Gérard, *RSC Adv.*, 2016, **6**, 114235–114243.
- 35 P. Banerjee, S. Kumar and S. Bose, *ACS Appl. Nano Mater.*, 2021, **4**, 6821–6831.
- 36 L. Hammer, N. J. Van Zee and R. Nicolaÿ, *Polymers*, 2021, **13**, 396.
- 37 P. Chakma and D. Konkolewicz, *Angew. Chem.*, 2019, **131**, 9784–9797.
- 38 J. M. Schuster, C. E. Schvezov and M. R. Rosenberger, *Procedia Mater. Sci.*, 2015, **8**, 732–741.
- 39 R. Rohini, K. Verma and S. Bose, *ACS Omega*, 2018, **3**, 3974–3982.
- 40 Y. Nassho and K. Sanada, *J. Compos. Mater.*, 2021, **55**, 27–38.
- 41 A. Susa, J. Bijleveld, M. Hernandez Santana and S. J. Garcia, *ACS Sustainable Chem. Eng.*, 2018, **6**, 668–678.
- 42 H. Memon and Y. Wei, *J. Appl. Polym. Sci.*, 2020, **137**, 1–10.
- 43 D. He, Z. Peng, W. Gong, Y. Luo, P. Zhao and L. Kong, *RSC Adv.*, 2015, **5**, 11966–11972.
- 44 I. A. Vacchi, C. Spinato, J. Raya, A. Bianco and C. Ménard-Moyon, *Nanoscale*, 2016, **8**, 13714–13721.
- 45 S. Verma and R. K. Dutta, *RSC Adv.*, 2015, **5**, 77192–77203.

- 46 C. R. Minitha and R. T. Rajendrakumar, *Adv. Mater. Res.*, 2013, **678**, 56–60.
- 47 M. Sahoo, R. P. Antony, T. Mathews, S. Dash and A. K. Tyagi, *AIP Conf. Proc.*, 2013, 1262–1263.
- 48 R. N. Muthu, S. Rajashabala and R. Kannan, *AIP Conf. Proc.*, 2018, 050107.
- 49 A. Sumisha, G. Arthanareeswaran, A. F. Ismail, D. P. Kumar and M. V. Shankar, *RSC Adv.*, 2015, **5**, 39464–39473.
- 50 C. Sun, Y. Zhang, P. Wang, Y. Yang, Y. Wang, J. Xu, Y. Wang and W. W. Yu, *Nanoscale Res. Lett.*, 2016, **11**, 110.
- 51 Z. Sun, F.-L. Guo, X.-P. Wu, Y.-Q. Li, W. Zeng, Q. Chen, T. Huang, P. Huang, Y.-Q. Fu, X.-Y. Ma, N. Hu and S.-Y. Fu, *Compos. Sci. Technol.*, 2022, **218**, 109166.
- 52 P. Sawai, P. P. Chattopadhyaya and S. Banerjee, *Mater. Today: Proc.*, 2018, **5**, 9989–9999.
- 53 C. Bao, Y. Guo, L. Song, Y. Kan, X. Qian and Y. Hu, *J. Mater. Chem.*, 2011, **21**, 13290.
- 54 B. Qiu, X. Zhang, S. Xia, T. Sun, Y. Ling, S. Zhou, H. Guang, Y. Chen, Z. Xu, M. Liang and H. Zou, *Composites, Part A*, 2022, **155**, 106811.
- 55 S. Wang, T. Wang, S. Zhang, Z. Dong, V. S. Chevali, Y. Yang, G. Wang and H. Wang, *Composites, Part B*, 2023, **251**, 110470.
- 56 J. M. Schuster, C. E. Schvezov and M. R. Rosenberger, *Procedia Mater. Sci.*, 2015, **8**, 732–741.
- 57 F. Liu, Z. Shi and Y. Dong, *Composites, Part A*, 2018, **112**, 337–345.
- 58 B. Qiu, X. Zhang, S. Xia, T. Sun, Y. Ling, S. Zhou, H. Guang, Y. Chen, Z. Xu, M. Liang and H. Zou, *Composites, Part A*, 2022, **155**, 106811.
- 59 I. Sengupta, S. Chakraborty, M. Talukdar, S. K. Pal and S. Chakraborty, *J. Mater. Res.*, 2018, **33**, 4113–4122.
- 60 X. Kong, F. Teng, H. Tang, L. Dong and Z. Feng, *Polymer*, 1996, **37**, 1751–1755.
- 61 X. Xu, W. Yuan, P. Liu, L. Liu, Y. Huang and Z. Hu, *Polym. Compos.*, 2023, **44**, 3095–3105.
- 62 C. Fang, J. Wang and T. Zhang, *Appl. Surf. Sci.*, 2014, **321**, 1–9.
- 63 S. Deng, X. Zhou, C. Fan, Q. Lin and X. Zhou, *Composites, Part A*, 2012, **43**, 990–996.
- 64 A. Azevedo do Nascimento, F. Fernandez, F. S. da Silva, E. P. C. Ferreira, J. D. D. Melo and A. P. Cysne Barbosa, *Composites, Part A*, 2020, **137**, 106016.
- 65 B. Chen, H. Cai, C. Mao, Y. Gan and Y. Wei, *Polym. Compos.*, 2022, **43**, 3124–3135.
- 66 M. Li, G. Zhao, X. Liu, X. Xie, C. Zhang, H. Yu, X. Jian, Y. Song and J. Xu, *Compos. Commun.*, 2023, **40**, 101631.
- 67 Y. Petronyuk, E. Morokov, V. Levin, T. Ryzhova, A. Chernov, V. Sherbakov and A. Shanygin, *Polym. Eng. Sci.*, 2017, **57**, 703–708.
- 68 Y. Petronyuk, V. Levin, S. Titov and T. Ryzhova, *J. Phys.: Conf. Ser.*, 2020, 045003.
- 69 N. J. Bongiardina, S. M. Soars, M. Podgorski and C. N. Bowman, *Polym. Chem.*, 2022, **13**, 3991–4003.
- 70 B. T. Michal, C. A. Jaye, E. J. Spencer and S. J. Rowan, *ACS Macro Lett.*, 2013, **2**, 694–699.
- 71 A. Ruiz de Luzuriaga, R. Martin, N. Markaide, A. Rekondo, G. Cabañero, J. Rodríguez and I. Odriozola, *Mater. Horiz.*, 2016, **3**, 241–247.
- 72 W. Denissen, J. M. Winne and F. E. Du Prez, *Chem. Sci.*, 2016, **7**, 30–38.
- 73 S. T. Kotikalapudi, R. Akula and R. P. Singh, *Composites, Part B*, 2022, **233**, 109516.
- 74 A. E. Zantout and O. I. Zhupanska, *Composites, Part A*, 2010, **41**, 1719–1727.
- 75 V. B. Mohan, R. Brown, K. Jayaraman and D. Bhattacharyya, *Mater. Sci. Eng., B*, 2015, **193**, 49–60.
- 76 J. D. Renteria, S. Ramirez, H. Malekpour, B. Alonso, A. Centeno, A. Zurutuza, A. I. Cocemasov, D. L. Nika and A. A. Balandin, *Adv. Funct. Mater.*, 2015, **25**, 4664–4672.
- 77 B. Alemour, H. N. Lim, M. H. Yaacob, O. Badran and M. Roshdi Hassan, *Mater. Res. Express*, 2019, **6**, 065607.
- 78 N. Ucar, B. K. Kayaoğlu, A. Bilge, G. Gurel, P. Sencandan and S. Paker, *J. Compos. Mater.*, 2018, **52**, 3341–3350.
- 79 Y. Li, Y. Zhao, J. Sun, Y. Hao, J. Zhang and X. Han, *Polym. Compos.*, 2016, **37**, 2494–2502.
- 80 D. D. L. Chung, *Carbon*, 2012, **50**, 3342–3353.
- 81 R. Sengupta, S. Mandal, A. Malakar, S. Rege, S. Islam, K. Samanta, A. Misra and S. Bose, *J. Mater. Chem. A*, 2023, **12**, 321–334.
- 82 S. Mandal, S. Sethi and K. Biswas, *J. Appl. Polym. Sci.*, 2023, **140**, DOI: [10.1002/app.53438](https://doi.org/10.1002/app.53438).
- 83 K. Manna, R. Sen Gupta, S. Mandal, A. Swaminadhan, S. Dutta, K. Samanta, Sk S. Islam, A. Malakar and S. Bose, absorption, *J. Mater. Chem. C*, 2023, **11**, 14725–14745.